Supplementary Information

Deep Learning Model for Inverse Design of Semiconductor Heterostructures with Desired Electronic Band Structures

Artem K Pimachev[1] and Sanghamitra Neogi[1,*]

[1] *Ann and H.J. Smead Aerospace Engineering Sciences, University of Colorado Boulder, Boulder, Colorado 80303, USA*

(Dated: January 31, 2023)

I. ATOMICALLY RESOLVED SPECTRAL FUNCTIONS OF SUPERLATTICES

Figure 1 shows spectral functions (SFs) of (a) bulk Si and (b) bulk Ge, and the progression of SFs of representative Si/Ge superlattices with decreasing period: (c) $Si_{26}Ge_{26}$, (d) $Si_{20}Ge_{20}$, (e) $Si_{12}Ge_{12}$, (f) Si_6Ge_6, and (g) Si_4Ge_4, respectively. The first column (i) represents the total SF and the columns (ii) and (iii) represent ASFs for atoms in the inner Si regions (red) and the inner Ge atoms (blue) of the superlattices, respectively. We show the inner Si and the Ge ASFs separately, to highlight how ASF differs for different atoms within the same superlattice. We compute ASFs for each atom in the superlattices and include in the training data. The results displayed in columns (ii) and (iii) of rows (c)-(h) represent the training data used in our forward ML models. The SFs are shown along $X-\Gamma-K-X$ path in the BZ of the reference cells, respectively. Representative BZ and the symmetry path are illustrated in Fig. 6 in the Methods section. We leverage the ML framework to average over the ASFs for each atomic environment in the training superlattices. We hypothesize that these data encompass the information needed to relate atomic environments in superlattices and resulting evolution of the band characters.

It is expected that the unfolded superlattice bands will display an average character of the folded bulk Si and Ge bands [1]. The total SF of $Si_{26}Ge_{26}$ superlattice in panel (c-i), displays a mixture bulk Si and Ge band characters. Similar observation can be made for the total SF of $Si_{20}Ge_{20}$ as well. However, it is interesting to note that the inner Si ASFs (c-ii, d-ii) of these two large period superlattices ($Si_{26}Ge_{26}$ and $Si_{20}Ge_{20}$) retain prominent bulk Si character. Similarly, the inner Ge ASFs (c-iii, d-iii) retain bulk Ge character. In general, these results show that the inner atom ASFs in large period superlattices primarily maintain the bulk band character and do not display a mixed character. However, we can identify the distinguishing characters of the superlattice bands (e.g., spitting or mixing of bands), upon a closer comparison between inner ASFs and bulk SFs. We discuss the comparison between bulk Si SF and inner Si ASFs. However, similar analysis can be done for Ge as well.

Splitting of bands: The inner ASFs of both $Si_{26}Ge_{26}$ and $Si_{20}Ge_{20}$ exhibit splitting of the bulk-like bands, especially near the Γ point. The degeneracy of the valence-band maxima at the Γ point is lifted and the bands are split. In an earlier publication, we illustrated that lattice strain in superlattices induces splitting of the valence bands, using Si_4Ge_4 as

* sanghamitra.neogi@colorado.edu

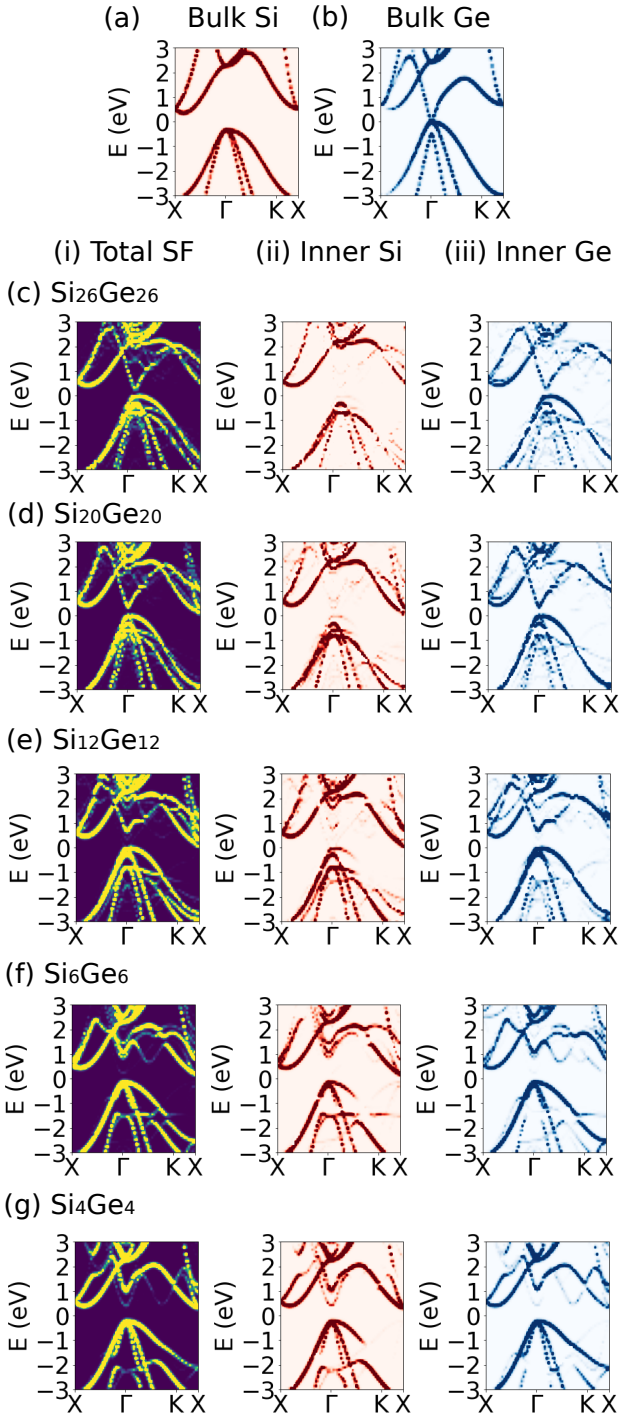

FIG. 1. **Example spectral functions (SFs) of Si/Ge systems investigated in this work:** SFs of bulk (a) Si and (b) Ge. (i) Total SFs and ASFs of (ii) inner Si and (iii) inner Ge atoms in (c) $Si_{26}Ge_{26}$, (d) $Si_{20}Ge_{20}$, (e) $Si_{12}Ge_{12}$, (f) Si_6Ge_6 and (g) Si_4Ge_4 superlattices.

an example [2]. Strain originates due to the lattice mismatch between Si and Ge layers as well as due to growth substrates. The threefold degenerate states that form the bulk Si valence band maximum split into two approximately degenerate p_x, p_y states and one nondegenerate p_z state [1, 3, 4]. The p_x, p_y states form the valence-band edge in Si_4Ge_4 and the p_z state splits off [2]. The band splittings exhibited by the ASF of $Si_{26}Ge_{26}$ and other superlattices are induced similarly by lattice strain. However, the order of the split states and the magnitude of the splitting depends on the specific strain environments. Additionally, Si and Ge layers experience different strains in a given superlattice. This causes leading to different strain induced band splittings for Si and Ge valence bands, as can be noted from (c-ii) and (c-iii). Valence band splittings are also exhibited by $Si_{12}Ge_{12}$ and other short-period superlattices. The conduction bands of short-period superlattices show splittings near the Γ point. Figure 1 illustrates the direct relationship between lattice strain environments and character of superlattice bands such as band splitting.

Mixing of bands and avoided crossing: The plots also illustrate that the valence bands of the superlattices exhibit a mixed Si-Ge character. This can be particularly noted from the ASFs of $Si_{12}Ge_{12}$ and Si_6Ge_6, shown in rows (e) and (f), respectively. The inner Si ASFs of these superlattices do not display band dispersions around -1 eV energy level, along the path $\Gamma - K$. However, the total SFs show continuous dispersions in this region. Upon considering column (iii), it can be concluded that the Ge bands mostly contribute to the total SFs in this region. The effect of strain on this mixed bands is complex. Varied strain environments in Si and Ge layers modulate the Si and Ge contributions differently. As can be noted from (e-ii) and (e-iii), the gaps between valence band edge and split-off states are different for Si and Ge ASFs. These split-off bands then affect each other. The split-off Si bands of $Si_{12}Ge_{12}$ and Si_6Ge_6 superlattices exhibit signature of avoided crossing due to the split-off Ge bands. The splittings are larger for smaller period superlattices and the indication of avoided crossing is more pronounced. Signatures of avoided crossing can be noted from the conduction bands of Si_6Ge_6 and Si_4Ge_4 superlattices, midway along $X - \Gamma$ and $\Gamma - K - X$ paths.

Folding of bands: The reference cells are mathematical constructions and may not represent true irreducible cells for a given heterostructure or superlattice. When the chosen reference cells do not capture full translational symmetry of the supercells, some residual folded bands are likely to appear. For example, signature of folded bands can be observed

along with band discontinuities in ASFs of Si_4Ge_4 superlattice, as shown in Fig. 1(g). This characteristics is particularly visible for short-period superlattices, with strong translational symmetry breaking. The comparison of the band dispersions along $X - \Gamma$ and $\Gamma - K - X$, reveals that ASFs experience more changes along the later symmetry direction. This can be understood by considering the BZ of the reference cell presented in Fig. 6 in the Methods section. The $\Gamma - K - X$ path spans two BZs. Therefore, varied contributions are expected to result in a range of features.

Change of Γ*-character:* The Γ-character of the bands of the large period superlattices (rows (c) and (d)) is primarily determined by Ge contributions. As the layer thickness decreases to 12 monolayers or below, the Γ-character is influenced by mixing of bands. For example, the top valence band of $Si_{12}Ge_{12}$ superlattice displays a partial Si and partial Ge character. Additionally, the contribution to the conduction bands is increasingly mixed near the Γ point, as can be seen from the ASFs of Si_6Ge_6 (row (f)) and Si_4Ge_4 (row (g) superlattices. These results demonstrate that the Γ-character of the superlattice bands strongly depends on the composition. A continuous band mixing has been demonstrated both theoretically and experimentally for alloys [5]. Here, we illustrate the band mixing for layered heterostructured Si-Ge systems. The progression SF plots further suggest that a direct band gap system can thus be designed by tuning the Γ-character. Earlier studies have identified that Si_6Ge_6 superlattice shows nearly direct band gap [6] while Si_6Ge_4 has a direct band gap [7]. We analyze the band structures along a specific symmetry path, therefore, precise identification of the direct or indirect nature of the band gap is out of scope for the present study. Identifying a direct band gap configuration from two indirect band gap materials promises various practical benefits, however, can be challenging [6, 7]. Although designing such a system is not the objective of our current study, Fig. 1 shows how our ML assisted first-principles modeling approach can be employed to achieve such a goal.

Figure 1 illustrates how ASFs of strain symmetrized superlattices change due to the decrease of superlattice periods. The strain induced band splittings, mixing of bands, avoided crossings and changes of Γ-character are dominant characters displayed by the ASFs of short-period superlattices. These features provide a measure to differentiate the superlattice and the bulk bands. Quantifying these characters is critical both from the fundamental viewpoint and for materials design for target applications. Our approach establishes a direct relationship between atomic environments and these band characters for complex heterostructures.

II. COMPARISON OF FORWARD MODEL PREDICTIONS & DFT RESULTS

Figure 2 shows the forward model-predicted SFs for the strain-symmetrized configuration of a $Si_{28}Ge_{28}$ superlattice. This structure is outside the training set, which include $Si_{26}Ge_{26}$ superlattice as the largest superlattice. We show the supercell configuration in Fig. 2(a). The SFs are predicted along the $X-\Gamma-K-X$ path of the Brillouin zone of the reference cell, with similar k and E resolution as training data. Figure 2(b) shows total SFs and the bottom rows show the ASFs of atoms from four regions of interest: (c) inner Si, (d) interface Si, (e) interface Ge, and (f) inner Ge. The different regions are indicated in the supercell with black circles (Fig. 2(a)). The total SFs are obtained by summing over the predicted ASFs of all atoms. The first and the second column of Fig. 2 show the ASFs predicted by the NN and the RF models, respectively. We compare the ML predictions with DFT results, shown in the third column and validate the predictions. We show the comparison between predicted and computed $I_n(E)$'s in the last column of Fig. 2 and report the MAEs.

The predicted total SFs display a mixture of Si-like and Ge-like characters, similar to DFT results, resulting in small MAEs (NN:0.08, RF:0.07). The presence of bulk-like character is similar to other large period superlattices. The predicted inner Si ASFs match with DFT results closely, yielding the smallest MAE 0.06 (Fig. 2(c)). In comparison, the DFT result of the inner Ge ASF exhibits splitting of the bulk-like bands, especially for the valence bands, near Γ point (Fig. 2(f)). The split band is less dispersive in the $\Gamma-K$ direction. The conduction band shows a small degree of splitting as well. These features are not captured in the NN prediction, resulting in a high MAE (0.27). Although the RF prediction cannot capture the splitting of the valence bands well, other bulk-like features are relatively well predicted, resulting in a smaller MAE: 0.10.

Meanwhile, the interface Si ASFs are considerably different from their bulk counterparts (Fig. 2(d,e)). For example, a larger contribution of Ge-like bands can be noted in DFT results, compared to the inner Si ASF. However, it is interesting to note that the Si and Ge DFT interface ASF results are quite similar to each other. Both of them display a mixed character strongly influenced by strain. The interface ASFs exhibit significantly more band splitting compared to inner ASFs. The splitting is related to the varied strain environments near interface. The strain induced splittings are more pronounced for the valence bands. The split-off valence bands are comparatively flat near the Γ point. Both the NN and the

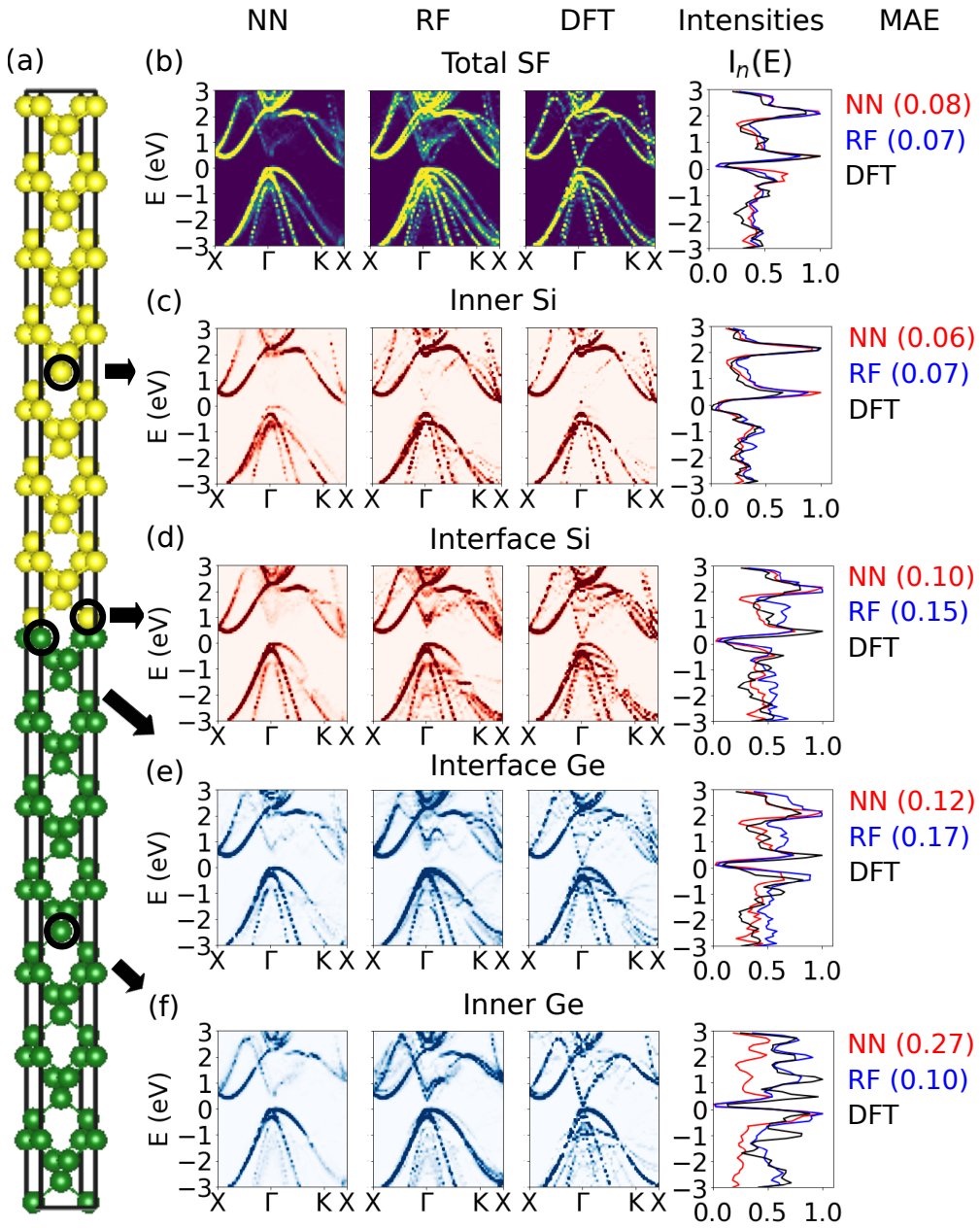

FIG. 2. **Total and atomically resolved spectral functions (SFs) of $Si_{28}Ge_{28}$ superlattice:** (a) Representative supercell configuration; (b) Total SF and ASFs of representative atoms in (c) inner Si region, (d) interface Si region, (e) interface Ge region, and (f) inner Ge region of the superlattice. NN and RF model predictions are shown in the first and second column of rows (b)-(f), respectively. Third column shows DFT results. Last column shows normalized intensities, $I_n(E)$, and MAEs between predicted and computed $I_n(E)$.

RF model fail to capture the finer details, however, they predict an average character of the strain-split bands. Although the predicted and computed ASFs show differences, it is interesting to note that the total SFs exhibit similar patterns.

III. EFFECTS OF FERMI-LEVEL ALIGNMENT

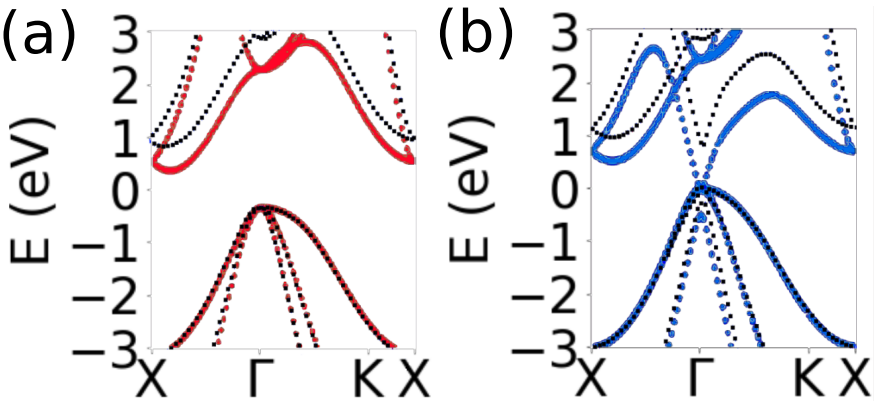

FIG. 3. **Band structures** of (a) bulk Si and bulk Ge obtained with PBE-GGA approach (solid lines). The dotted black lines represent results from GW calculation from literature [8].

It is known that the PBE-GGA approach fails to predict semiconductor band gaps accurately, as is particularly evident from Fig. 1(b). We show a comparison between PBE-GGA band structures and those obtained with GW calculations [8] (black dashed line) in Fig. 3. The valence bands obtained with the PBE-GGA approach match the GW results, however, the conduction bands are lowered resulting in an underestimated band gap. Such discrepancy has been discussed extensively [2, 9–12]. Nevertheless, the PBE-GGA approach has been extensively used to predict the electron/hole transport properties of semiconductors, including the biaxial strain enhanced in-plane mobility in Si [13] and thermoelectric properties of Si [14, 15] and Si/Ge superlattices [2, 12, 16–19]. In previous publications, we compared the electronic transport properties [2] predicted using the PBE functionals and the Heyd-Scuseria-Ernzerhof [20]. Through a systematic analysis we illustrated the effectiveness of PBE-GGA approach to predict the relationship between lattice environment and electronic properties of semiconductor heterostructures. In this article, our objective is to develop a model for rapid prediction of this relationship. The computational cost of the

alternative approaches such as using hybrid functionals [21, 22] or implementing GW calculations [8] prohibits the use of these approaches to analyze large structures, especially for data driven studies. Additionally, The prior studies provide necessary justification to use PBE-GGA approach to establish the model.

Here, we use data obtained with PBE-GGA approach to train ML models. We discuss the role of Fermi-level alignments on ML predictions. To obtain the results shown in main manuscript, we use one Fermi level alignment for the forward learning level, but different Fermi level alignments for the reverse learning model.

Forward Learning Approach: We assign the Fermi-level ($E = 0$ level) to be equal to the middle of the bandgap value, to obtain the total SF for each training configuration. The ASF energy bands are shifted by the corresponding amount. The forward learning model is trained with the resulting ASFs. We show the predicted ASFs and total SFs of test superlattices and heterostructures in Fig. 2 and Fig. 2 of main manuscript, respectively. As can be seen from the figures, both predicted energy bands and energy level alignments are in good agreement with the corresponding DFT results.

Different Fermi-level Alignments: We illustrate the change of ML predictions by varying alignments of training ASFs.

(Case I) Electronic band gap cannot be directly defined for the ASFs, to the best of our knowledge. We align the Fermi-level of each ASF of training superlattice to the respective mid-band-gap level. We task the trained ML model to predict ASF (or total SF in this case) for bulk Si systems. Bulk systems include atomic environments which is not present in the training structure that includes a mixture of both the materials. As we illustrate below, the Fermi-level alignment strongly affects the predictions in this case. Figure 4 shows the SFs of (a) relaxed and (b) strained Si. The systems are modeled with tetragonal supercells that include four Si atoms. The first and the second column show the SFs predicted by the NN and the RF models, respectively. The third column represents DFT results. We show the comparison between predicted and computed $I_n(E)$'s in the last column and report the MAEs. The mismatch between Fermi-levels is pronounced in the plot showing the normalized intensities for strain-symmetrized bulk Si. Interestingly, the predictions are in good agreement with the DFT SF results for bulk Si with in-plane strain.

(Case II) We align ASFs such that the zero-energy level of each ASF corresponds to the largest spectral weight at the Γ-point in the valence zone or valence band maximum

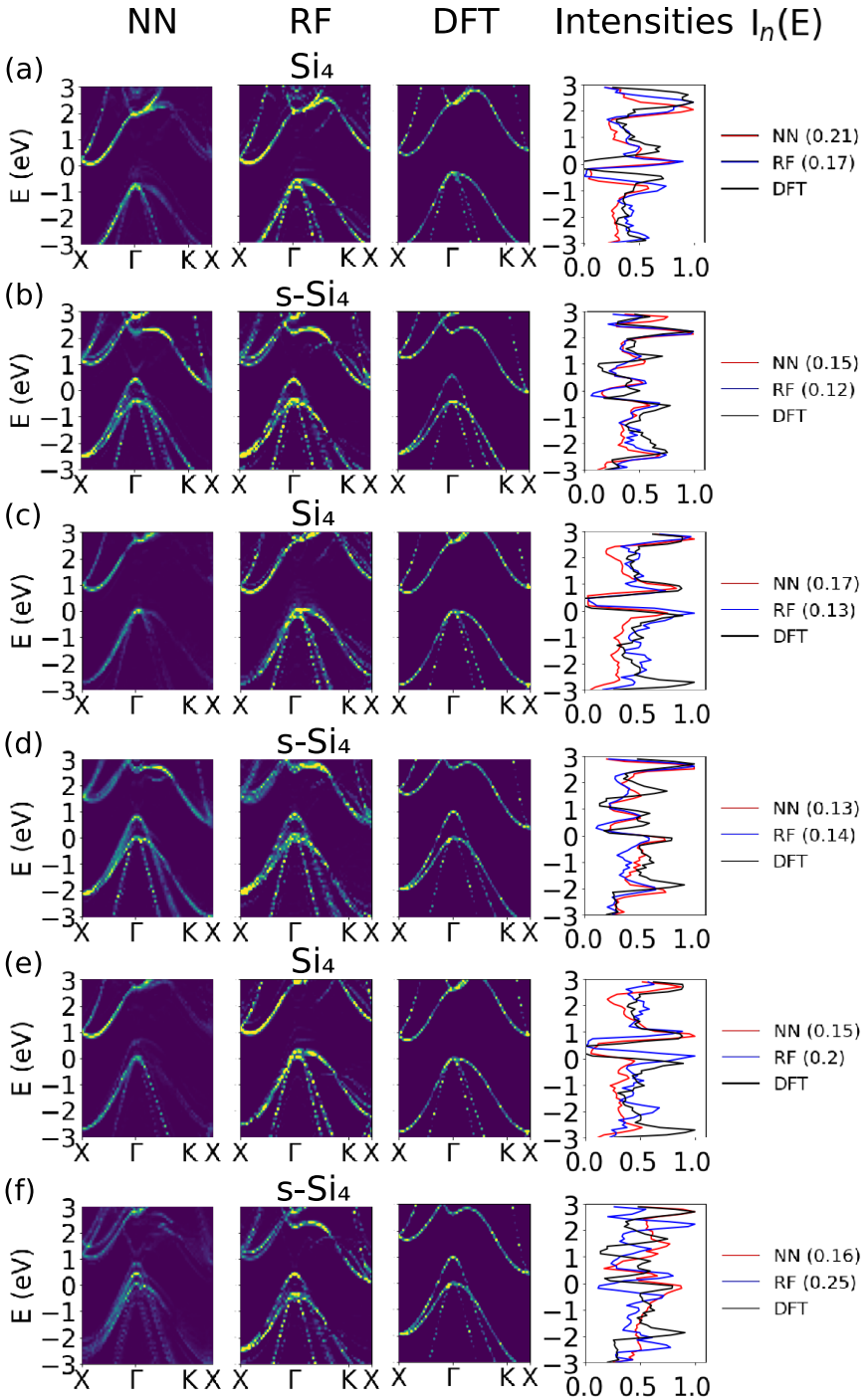

FIG. 4. **Effect of Fermi-level alignment of SF on ML performance:** (a-b) ASFs with Fermi-level aligned at the mid gap level. Predicted SFs for (a) relaxed bulk Si and (b) bulk Si in tensile strain due to Ge substrate. ASFs with Fermi-level aligned at VBM, independently for each ASF: Predicted SFs for (c) relaxed and (d) strained bulk Si. ASFs with Fermi-level aligned at VBM, independently for each total SF: Predicted SFs for (e) relaxed and (f) strained bulk Si.

(VBM). We retrain the model with VBM aligned-ASFs and task the model to predict ASFs for the bulk systems. The predictions are shown for relaxed and strained bulk Si systems in Fig. 4(c,d). In this case, both the peak intensities and the energy alignments are reproduced with a good agreement with DFT results.

(Case III) We align the total SF of each training superlattices such that the zero-energy level is set to the largest spectral weight at the Γ-point in the valence zone or VBM. The energy bands of ASFs are shifted by the corresponding amount. The ML predictions for the bulk systems are are shown in Fig. 4(e,f). The NN predicted relaxed Si bands are better aligned than RF, however the spectral weights are diminished for the NN predictions. The predictions for both relaxed and strained Si are worse that the ones reported for case (II).

As can be observed from above discussion, the ML predictions vary in an unpredictable manner depending on the energy level alignments of training ASFs. To generalize and diversify the training set for the reverse approach, we consider 13 Fermi level alignments in incremental steps in the range from +0.5 eV to -0.5 eV from the mid-gap energy level. The various alignments correspond to different electron doping in ARPES experiments.

Reverse Learning Approach: We test the CNN model to predict the descriptors of bulk Si systems when the SF images are provided as input. We use two categories of test images: the DFT predicted SFs of relaxed and strained bulk Si and a spectra obtained from ARPES experiment. In practice, only the valence bands may be available in the ARPES experimental images. To adapt to such constrains, we train the reverse ML model with the energy levels of DFT results below the VBM level. In other words, the ASFs are aligned individually such that the zero-energy level corresponds to the largest spectral weight at the Γ-point in the valence zone. As discussed above, the band gap is not directly defined for the ASF, so the shift in the Fermi level is ambiguous. This provides a way to expand the training data set by applying various amount of shifts. The CNN model is then trained on the corresponding ASFs. The CNN approach has shown high level of efficiency with image data sets. We expect the CNN model to capture unique patterns in the ASF rather than the shift associated with the different Fermi-level alignments.

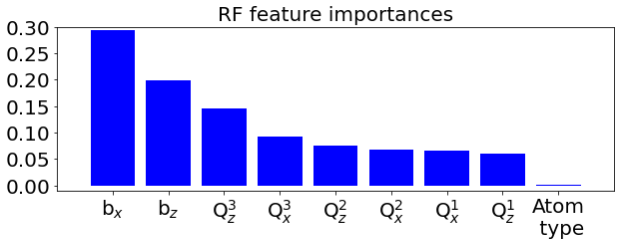

FIG. 5. RF feature importance

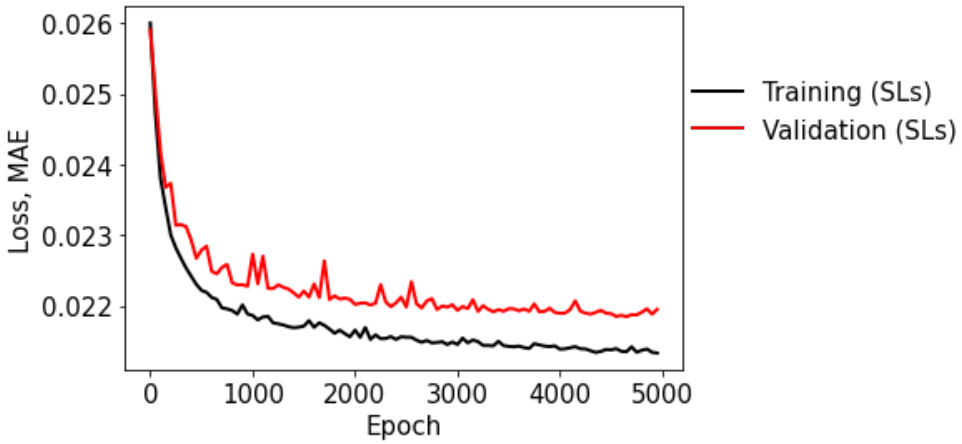

FIG. 6. Learning curves for NN.

IV. TRAINING FORWARD AND REVERSE ML MODELS

The feature importance for RF model is shown in Fig. 5. As shown in the figure, b_x has the highest importance as it is the measure of in-plane strain that induces band splittings. b_z is the next most important feature, that is responsible for internal interatomic distances due to different atom types in the configuration. Interestingly, the higher order parameters are of the higher importance, we attribute that to their long range sensitivity to the presence of material interfaces. Importance of the atom type seems diminished, which can be explained by the fact that only two atomic types are considered. The other features can distinguish the atomic environments indirectly. This, however, may change when many atomic species are present in the training configurations.

The learning curves during the training of forward NN and reverse CNN model are shown in Fig. 6 and Fig. 7, respectively. As the figure shows MAEs change as we change the number

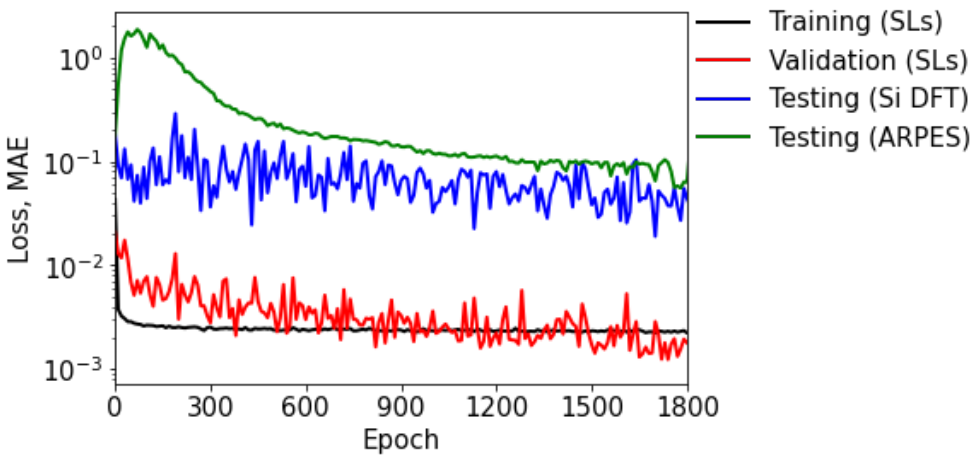

FIG. 7. Learning curves for CNN.

of epochs of the model. We select the epoch with lowest validation set MAE (red curves). In this article, we present the results obtained with epoch 4700 and 1750 for the forward NN and CNN model, respectively. However, choice of these numbers is arbitrary.

V. TEST OF REVERSE LEARNING MODEL

Heterostructure: We test the performance of the reverse learning model on the multilayer heterostructure, $Si_{24}Ge_{15}Si_9Ge_6Si_3Ge_3$. The chosen configuration is strain-symmetrized. We show the CNN-predicted descriptors for all atoms of the heterostructure in Fig. 8. Figure 4 of main manuscript shows the model performance on a strained configuration of the same heterostructure. The prediction error is higher for the strain-symmetrized configuration. We speculate that the higher error arises because the number of strain-symmetrized configurations is small in the training set compared to strained configurations.

Bulk systems: We consider bulk Si and bulk Ge models grown on $Si_{1-x}Ge_x$ substrate with varied concentrations, x, that induces four different strains: 0.00%, 0.59%, 1.16%, 1.73%. We refer to the strained Si and Ge as s-Si and s-Ge, respectively. It is important to note that the training set only includes superlattices and do not include any information about pristine bulk material. The bulk SFs are provided to the combined model as input. We show the CNN-predicted descriptors in Table 1. The CNN model predicts atom type= 1 (or type= 2) for all Si (or Ge) test structures. The model is able to perceive the absence of

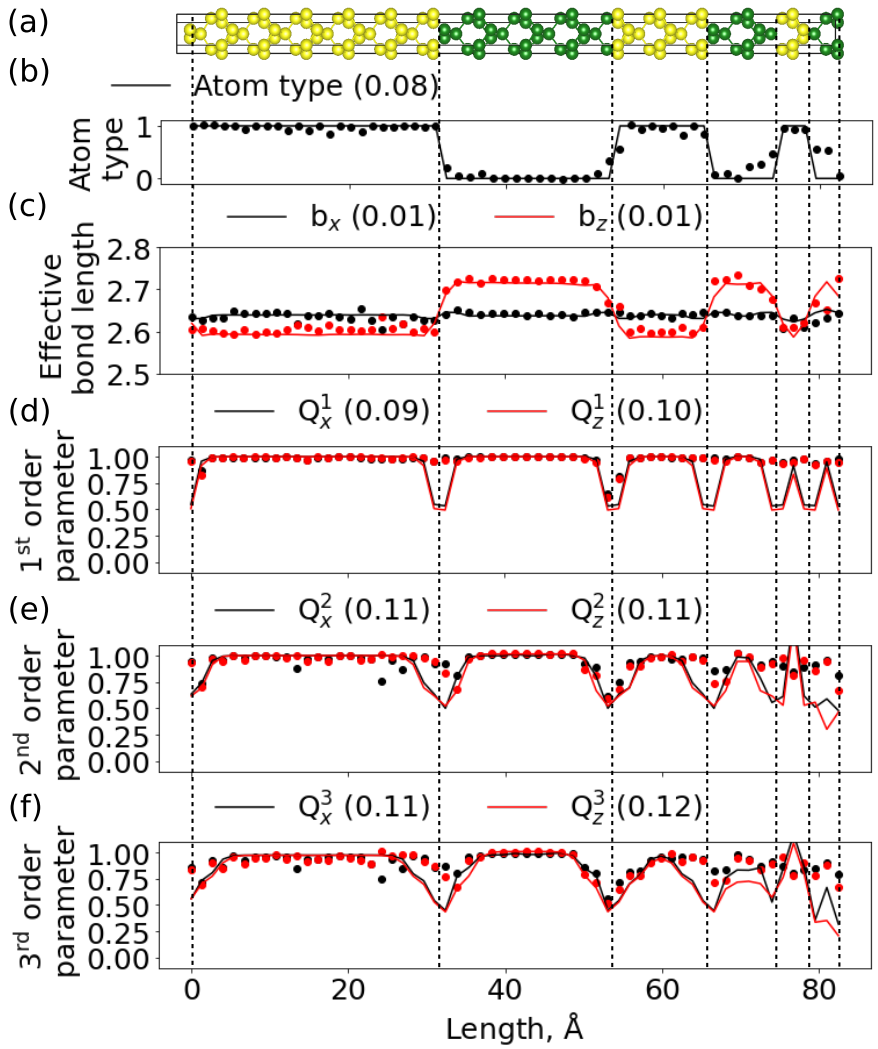

FIG. 8. **CNN predicted atomic environment descriptors of strain-symmetrized $\mathbf{Si_{24}Ge_{15}Si_9Ge_6Si_3Ge_3}$ heterostructure:** (a) Supercell configuration; Predicted (b) atom type, (c) effective bond length and (d-f) spatially resolved order parameters, Q_i^{order} where $i = (x, z)$ and $order = 1, 2, 3$. MAEs between predicted (circles) and calculated features (solid lines) are shown within parentheses, next to legends.

Ge (or Si), even though all ASF training data include Ge (or Si) signatures. The identical b_x and b_z are also accurately predicted for relaxed bulk Si and Ge. The applied in-plane strains directly affect the bond lengths. b_x's of increase with higher in-plane strain. To keep the volume constant, b_z decreases. It is remarkable that the predicted order parameters are all close to the bulk values (~ 1), even in highly strained systems. This result indicates that order parameters are highly effective in distinguishing mixed environments from pristine

TABLE 1. Computed and Predicted Si & Ge Descriptors

Test image	type	b_x	b_z	Q_x^1	Q_z^1	Q_x^2	Q_z^2	Q_x^3	Q_z^3
Si	DFT	1.00	2.58	2.58	1.00	1.00	1.00	1.00	1.00	1.00
	CNN	0.99	2.61	2.61	1.00	1.00	1.00	1.00	0.99	1.00
s-Si [1]	DFT	1.00	2.62	2.60	1.00	1.00	1.00	1.00	1.00	1.00
(0.59%)	CNN	1.00	2.61	2.61	1.00	1.00	1.00	1.00	0.97	0.97
s-Si [2]	DFT	1.00	2.61	2.57	1.00	1.00	1.00	1.00	0.97	0.97
(1.16%)	CNN	1.00	2.64	2.60	1.00	1.00	1.00	1.01	0.97	0.96
s-Si [3]	DFT	1.00	2.63	2.57	1.00	1.00	1.00	1.00	1.00	1.00
(1.73%)	CNN	1.00	2.64	2.59	0.99	1.00	1.00	1.00	0.98	0.97
Ge	DFT	0.00	2.73	2.73	1.00	1.00	1.00	1.00	1.00	1.00
	CNN	0.01	2.66	2.70	1.00	1.00	1.00	1.00	0.99	1.00
s-Ge [1]	DFT	0.00	2.60	2.81	1.00	1.00	1.00	1.00	1.00	1.00
(0.00%)	CNN	0.01	2.56	2.77	1.00	1.00	1.00	1.00	0.97	0.99
s-Ge [2]	DFT	0.00	2.61	2.80	1.00	1.00	1.00	1.00	1.00	1.00
(0.59%)	CNN	0.01	2.58	2.76	1.00	1.00	1.00	1.00	0.97	0.99
s-Ge [3]	DFT	0.00	2.62	2.80	1.00	1.00	1.00	1.00	1.00	1.00
(1.16%)	CNN	0.01	2.59	2.76	1.00	1.00	1.00	1.00	0.98	0.99
s-Ge [4]	DFT	0.00	2.63	2.79	1.00	1.00	1.00	1.00	1.00	1.00
(1.73%)	CNN	0.01	2.60	2.75	1.00	1.00	1.00	1.00	0.98	0.99

ones. Figure 5 in main article shows the comparison between $I_n(E)$, computed from the output of the combined forward-reverse model and DFT data for two Si systems. We find a good agreement between predicted and computed normalized intensities for all systems.

[1] S. Satpathy, R. M. Martin, and C. G. Van de Walle, Electronic properties of the (100)(si)/(ge) strained-layer superlattices, Physical Review B **38**, 13237 (1988).

[2] V. S. Proshchenko, M. Settipalli, A. K. Pimachev, and S. Neogi, Role of substrate strain to tune energy bands–seebeck relationship in semiconductor heterostructures, Journal of Applied Physics **129**, 025301 (2021).

[3] M. S. Hybertsen and M. Schlüter, Theory of optical transitions in si/ge (001) strained-layer superlattices, Physical Review B **36**, 9683 (1987).

[4] C. Tserbak, H. Polatoglou, and G. Theodorou, Unified approach to the electronic structure of strained si/ge superlattices, Physical Review B **47**, 7104 (1993).

[5] T. D. Eales, I. P. Marko, S. Schulz, E. O'Halloran, S. Ghetmiri, W. Du, Y. Zhou, S.-Q. Yu, J. Margetis, J. Tolle, *et al.*, Ge1- xsnx alloys: consequences of band mixing effects for the evolution of the band gap γ-character with sn concentration, Scientific reports **9**, 1 (2019).

[6] S. Froyen, D. Wood, and A. Zunger, Structural and electronic properties of epitaxial thin-layer si n ge n superlattices, Physical Review B **37**, 6893 (1988).

[7] M. d'Avezac, J.-W. Luo, T. Chanier, and A. Zunger, Genetic-algorithm discovery of a direct-gap and optically allowed superstructure from indirect-gap si and ge semiconductors, Physical review letters **108**, 027401 (2012).

[8] Y.-M. Niquet, D. Rideau, C. Tavernier, H. Jaouen, and X. Blase, Onsite matrix elements of the tight-binding hamiltonian of a strained crystal: Application to silicon, germanium, and their alloys, Physical Review B **79**, 245201 (2009).

[9] J. P. Perdew, Density functional theory and the band gap problem, International Journal of Quantum Chemistry **30**, 451 (1986).

[10] J. P. Perdew, W. Yang, K. Burke, Z. Yang, E. K. Gross, M. Scheffler, G. E. Scuseria, T. M. Henderson, I. Y. Zhang, A. Ruzsinszky, *et al.*, Understanding band gaps of solids in generalized kohn–sham theory, Proceedings of the National Academy of Sciences **114**, 2801 (2017).

[11] Á. Morales-García, R. Valero, and F. Illas, An empirical, yet practical way to predict the band gap in solids by using density functional band structure calculations, The Journal of Physical Chemistry C **121**, 18862 (2017).

[12] V. S. Proshchenko, M. Settipalli, and S. Neogi, Optimization of seebeck coefficients of strain-symmetrized semiconductor heterostructures, Applied Physics Letters **115**, 211602 (2019).

[13] D. Yu, Y. Zhang, and F. Liu, First-principles study of electronic properties of biaxially strained silicon: Effects on charge carrier mobility, Physical Review B **78**, 245204 (2008).

[14] N. F. Hinsche, I. Mertig, and P. Zahn, Effect of strain on the thermoelectric properties of

silicon: an ab initio study, Journal of Physics: Condensed Matter **23**, 295502 (2011).

[15] V. S. Proshchenko, P. P. Dholabhai, T. C. Sterling, and S. Neogi, Heat and charge transport in bulk semiconductors with interstitial defects, Physical Review B **99**, 014207 (2019).

[16] N. Hinsche, I. Mertig, and P. Zahn, Thermoelectric transport in strained si and si/ge heterostructures, Journal of Physics: Condensed Matter **24**, 275501 (2012).

[17] M. Settipalli and S. Neogi, Theoretical prediction of enhanced thermopower in n-doped si/ge superlattices using effective mass approximation, Journal of Electronic Materials **49**, 4431 (2020).

[18] M. Settipalli, V. S. Proshchenko, and S. Neogi, The effect of electron–phonon and electron-impurity scattering on the electronic transport properties of silicon/germanium superlattices, Journal of Materials Chemistry C **10**, 7525 (2022).

[19] A. K. Pimachev and S. Neogi, First-principles prediction of electronic transport in fabricated semiconductor heterostructures via physics-aware machine learning, npj Computational Materials **7**, 93 (2021).

[20] J. Heyd, G. E. Scuseria, and M. Ernzerhof, Hybrid functionals based on a screened coulomb potential, Journal of chemical physics **118**, 8207 (2003).

[21] K. Hummer, J. Harl, and G. Kresse, Heyd-scuseria-ernzerhof hybrid functional for calculating the lattice dynamics of semiconductors, Physical Review B **80**, 115205 (2009).

[22] C. Stephenson, W. O'Brien, M. Penninger, W. Schneider, M. Gillett-Kunnath, J. Zajicek, K. Yu, R. Kudrawiec, R. Stillwell, and M. Wistey, Band structure of germanium carbides for direct bandgap silicon photonics, Journal of Applied Physics **120**, 053102 (2016).